A dedicated powder diffraction beamline at the Advanced Photon Source: Commissioning and early operational results

Jun Wang,[a] Brian H. Toby, Peter L. Lee, Lynn Ribaud, Sytle M. Antao, Charles Kurtz, Mohan Ramanathan, Robert B. Von Dreele, and Mark A. Beno
Advanced Photon Source, Argonne National Laboratory, Argonne, Illinois 60439, USA

(Received 11 June 2008; accepted 21 July 2008; published online 22 August 2008)

A new dedicated high-resolution high-throughput powder diffraction beamline has been built, fully commissioned, and opened to general users at the Advanced Photon Source. The optical design and commissioning results are presented. Beamline performance was examined using a mixture of the NIST Si and Al_2O_3 standard reference materials, as well as the LaB6 line-shape standard. Instrumental resolution as high as 1.7×10^{-4} ($\Delta Q/Q$) was observed. © *2008 American Institute of Physics.* [DOI: 10.1063/1.2969260]

I. INTRODUCTION

Many of the most interesting materials being studied today are not available in single-crystal form during the critical period following the initial discovery, if ever. It is precisely during this initial phase that structural information is most critically needed. High-resolution powder diffraction thus provides a key research tool for determining the structure, for following the structural changes as a function of temperature, voltage, field, etc., and for defining future synthetic approaches to enhance desired materials properties, which may include conductivity, thermal expansion, biological activity, or chemical activity.[1–6] Increasingly complex chemistry and physics of modern materials demand that the structural information be obtained with high precision. The increased number of applications for powder diffraction crystallography demands these data be available in a routine fashion.

A dedicated high-resolution, high-throughput powder diffraction beamline, 11BM, was proposed, constructed, and commissioned at the Advanced Photon Source (APS) at Argonne National Laboratory to facilitate high-resolution crystallographic structure determination from powder diffraction of complex polycrystalline materials via a high-throughput mail-in service model. This beamline will support a wide range of user interests, from pharmaceuticals through traditional materials science to questions in engineering, catalysis, chemistry, geosciences, physics, and electronics.

II. BEAMLINE OPTICS

Beamline 11BM is built on a bending magnet source operating at an electron energy of 7 GeV with a critical photon energy of 19.5 keV. This beamline is designed to operate in the energy range of 5–40 keV and therefore can cover the *K* absorption edge for elements from Ti to La, and *L* absorption edges for elements above Cs for resonant scattering studies.

A schematic layout of the beamline is shown in Fig. 1. A 1-m-long mirror is located 26.0 m from the bending magnet source. It collimates beam vertically to minimize the energy spread of the monochromator and to reduce harmonics contamination. The mirror has one 50-mm-wide stripe coated in Pt and another 50 mm uncoated Si stripe. At a 2 mrad incident angle, the Pt-coated stripe has a cutoff energy at 40.5 keV, and the Si region at 15.5 keV. The mirror is water cooled, with liquid gallium/indium as the heat transfer medium, and is able to translate between the Pt stripe and the uncoated region of the Si to choose a different energy. The mirror acceptance is 50 mm horizontal (about 1.9 mrad) and 2 mm maximum vertical defined by upstream white beam slits located 23.4 m from the source. A manual mechanical bending mechanism allows the mirror to be bent cylindrically from a nearly flat profile to a curvature with a radius of approximately 26 km.

Following the collimating mirror, the x-ray beam is monochromated by a 20 mm fixed-exit double-crystal Si (111) monochromator positioned 27.6 m from the source. The first crystal is flat and water cooled, and the second crystal is sagittally bent to focus the beam horizontally. The sagittal focusing assembly was purchased from Oxford-Danfysik with the design licensed to Oxford-Danfysik from the ESRF. There is a gear reducer (28:1) and a positional readout linear variable differential transformer (LVDT) for each bender motor. The gear reducer increases the accuracy of the motion by a factor of 28 and enhances the torque necessary for high-energy operation; for example, the bending radius is 1.6 m at 30 keV. The LVDT acts as an encoder and allows us to move to positional values indicated by the LVDT readouts. This eliminates or significantly reduces any backlash problems.

The orientation of the second crystal may be adjusted with four degrees of freedom: a slide positions the second crystal relative to the first to maintain a constant beam displacement; a yaw control allows rotation around the crystal surface normal, which is crucial for compensating the twist of the sagittal crystal; the pitch control, which has both a motorized coarse adjustment and a piezoelectric fine adjust-

[a]Author to whom correspondence should be addressed. Electronic mail: junwang@bnl.gov.

 © 2008 American Institute of Physics

Downloaded 19 Sep 2008 to 164.54.111.19. Redistribution subject to AIP license or copyright; see http://rsi.aip.org/rsi/copyright.jsp

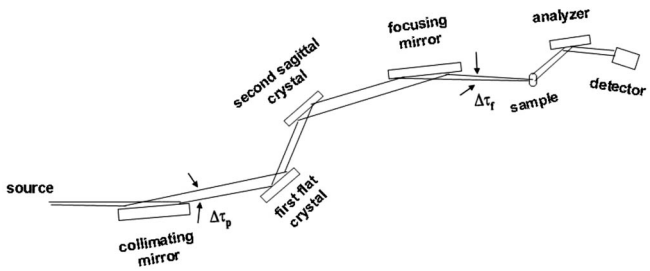

FIG. 1. Schematic layout of 11BM beamline optics.

ment, allows relative adjustment of the second crystal's Bragg angle with respect to the first; and a roll control tilts the crystal around the incident beam. For the purpose of equipment protection, thermocouples are placed on the first crystal, the pedestal supporting the second crystal, and most of the control motors.

A second uncooled mirror is situated downstream (29.9 m from the source) to focus the beam vertically in order to obtain high intensity. The dimensions and coating specifications of the second mirror replicate the first mirror. The bending radius can be adjusted manually to focus beam at the sample or detector position, which is about 50 m from the source.

To minimize the vertical divergence of the beam, the optical components are positioned to provide close to a 1:1 demagnification ratio for vertical focusing. Although 3:1 is the optimal demagnification ratio for sagittal focusing to ultimately satisfy the Bragg condition of the incident beam with horizontal divergence,[7] the investigation of the effect of the sagittal focusing on vertical divergence by ray tracing shows that the 3:1 ratio causes asymmetric and broadened distribution of the beam vertical divergence.[8] Since the highest resolution for powder diffraction is a driving goal for this beamline, the 1:1 demagnification ratio was chosen for the sagittal focusing to provide a symmetric and narrow vertical divergence distribution at the cost of a loss of intensity at a higher energy.

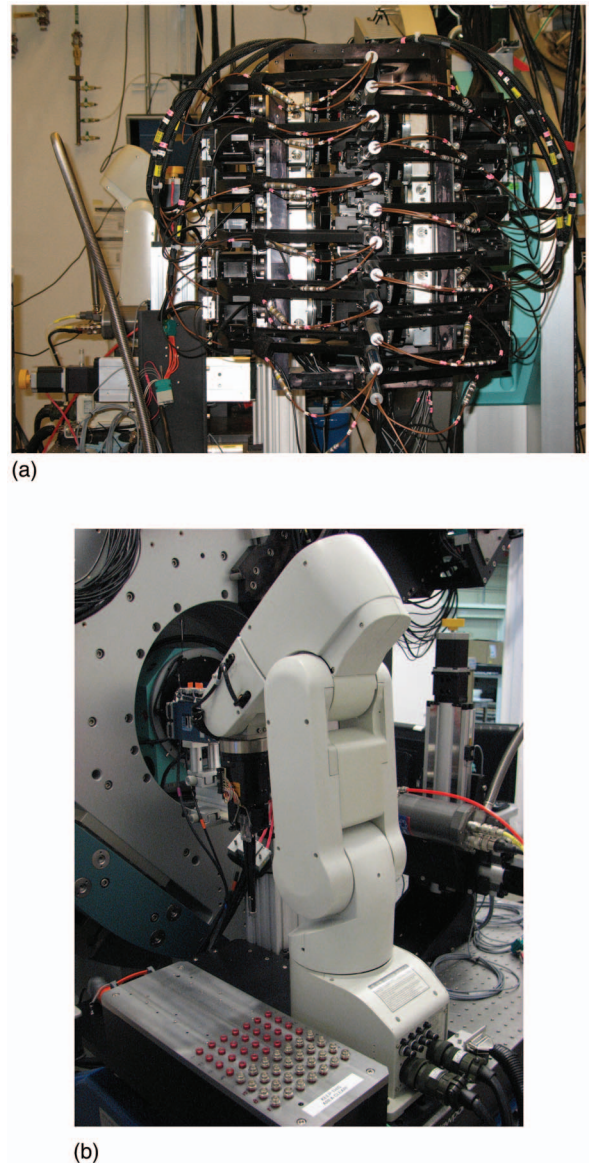

FIG. 2. (Color) Pictures of the 11BM (a) 12 analyzer/detector system and (b) robotic sample exchanger.

III. DIFFRACTOMETER

A Huber two-circle diffractometer is composed of two heavy-duty high-precision rotary tables (serving as 2θ and θ angles, respectively), each with a Heidenhain encoder that is aligned coaxially. The axis of rotation is horizontal. The high angular accuracy ($3\times10^{-4}\circ$) and high precision ($<10^{-5}\circ$) allow the diffraction patterns' peak positions to be accurate and reproducible. The diffractometer, the final beamline guard slits, and the ion chamber are mounted on a locally designed table that has motorized horizontal and vertical movements and manual rotation adjustability. With these motions the diffractometer axis can be centered and made perpendicular to the x-ray beam. A Newport optical table top is also attached on the diffractometer table to provide an area on which to mount the robotic sample changer, sample environmental devices, and other accessories. A sample stage with a high-speed sample spinner and three-axis translations allows alignment of the spinner axis to the diffractometer and transverse centering of the sample along the diffractometer axis. We have found that a 90 Hz spinning rate optimizes sample stability while offering reasonable powder averaging for our measurements, which may have count times as short as 0.01 s.

The multianalyzer/detector system is unique to this instrument. A brief description follows; a more comprehensive description will be published separately.[9] To achieve high angular resolution and data collection efficiently, 12 Si (111) crystal analyzer-detector systems are mounted on the diffractometer 2θ arm [Fig. 2(a)]. Each analyzer is spaced nominally 2° apart, so a 2° scan provides measurement of a 24° 2θ range. Each analyzer has an associated $LaCl_3$ (Cyberstar) scintillation detector. The multianalyzer/detector system is capable of adjusting each analyzer crystal's orientation on two axes. Each crystal's setting angle (θ) has both a coarse (mechanical) and a fine (piezodriven flexure) adjustment, which are computer controlled. The multianalyzer/detector scheme reduces greatly the data collection time, improves

Downloaded 19 Sep 2008 to 164.54.111.19. Redistribution subject to AIP license or copyright; see http://rsi.aip.org/rsi/copyright.jsp

data reliability by offering redundancy to confirm that measurements are internally consistent, and facilitates time-resolved experiments at high resolution. The detector module is also designed to prevent cross talk between the analyzer-detector systems. Two parallel slit sets, one before and one after each analyzer crystal, collimate and separate the diffracted x rays for each analyzer and its associated scintillation detector.

An experimental physics and industrial control system (EPICS)-based beamline control system has been adapted to allow continuous measurements as the 2θ angle is scanned, thus eliminating motor repositioning overhead. The 2θ positions and the integrated counts from the detector are written to VME memory by the scaler card. The VME memory is read by the instrument when the scan is finished. This allows the entire high-resolution powder diffraction pattern to be recorded in times as short as a few minutes, although a more typical data collection time is 1 h.

Another unique feature is the robotic sample exchanger. In order to achieve maximum efficiency and effectiveness, an automatic sample-exchange system has been built and integrated into the diffraction system. This system, shown in Fig. 2(b), exploits the high-throughput capability of this beamline. The locally designed fingers and interface hardware allow the commercial robot to mount, exchange, and dismount samples. The sample capacity of 120 samples can be expanded as needed. Integral to the design is an EPICS control module, which allows the robot to be interfaced as a standard beamline peripheral device, as well as a safety system that inhibits robotic operation where an operator could be endangered by the robot's rapid motion. High-throughput data collection is implemented using a combination of web-based database interface and Python instrument control scripts, which will be described elsewhere.[10]

An Oxford Cryostreams Cryostream 700+ device allows automated temperature control from 80 to 500 K to be integrated with robotic operation. Additional sample environmental control systems will be added at a later time.

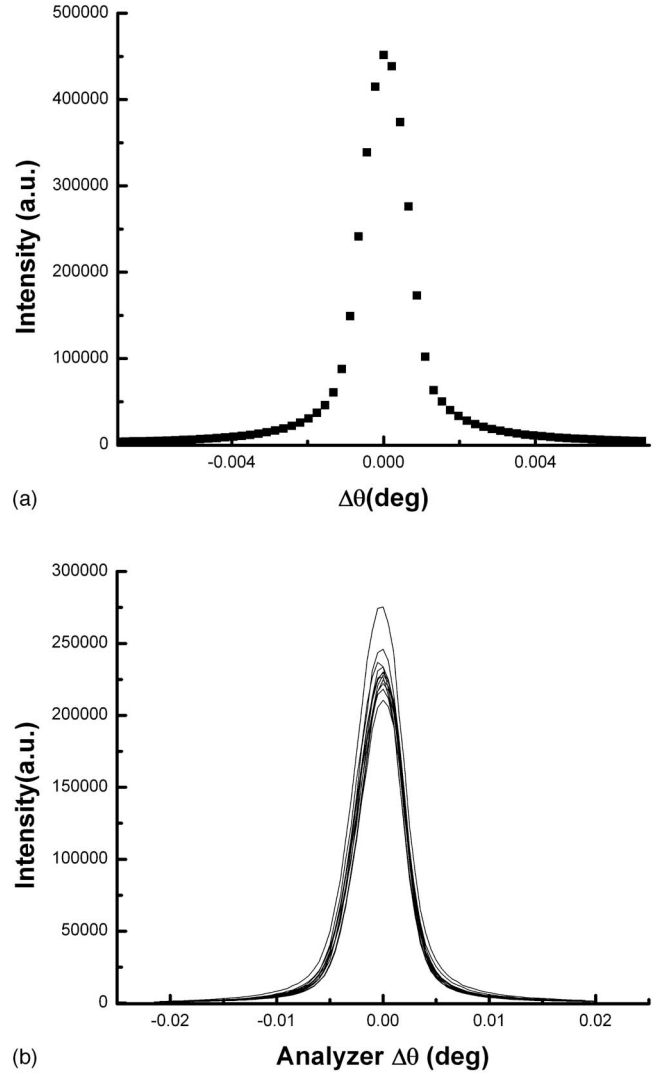

FIG. 3. Rocking curve widths at 30 keV: (a) Si (111) monochromotor crystal and (b) Si (111) analyzer crystal.

IV. COMMISSIONING RESULTS

The evaluation of beamline performance is based mainly on two criteria: the instrument resolution function (IRF), which summarizes the instrumental line profile as a function of diffraction angle 2θ, and the x-ray photon flux and focal size of the incident beam on the sample. In this section we present commissioning results from this beamline, with emphasis on diffractometer system performance.

A. Flux and focusing performance

The measured photon flux at 30 keV is 3×10^{11} photons/s at the sample position with 100 mA current. This compares well with the design value of 5.6×10^{11}, which includes the effects of mirror acceptance in both vertical and horizontal directions, reflectivities of both mirrors, and a 0.012% bandwidth of the Si (111) monochromator. The measured rocking curve of the monochromator at 30 keV is shown in Fig. 3(a). The rocking curve width of 4.5 arc sec, observed with the sagittal crystal fully focused, compares well with the calculated value of 2.7 arc sec at this energy for a pair of perfectly flat crystals according to x-ray oriented programs (XOP).[11] The broadening of the rocking curve width could be caused by the heat load on the first crystal, and the twist and strain from the sagittal crystal. The loss of the measured flux is consistent with the wider rocking curve width and therefore can be attributed to imperfections in the monochromator crystals.

Figure 4 shows focused horizontal and vertical beam profiles at the sample position measured by the slit scan. The full width at half maximum (FWHM) of the horizontal focal size is 360 μm. This is compared to the theoretical value of 242 μm. The reason for the discrepancy may be due to the ribbed sagittal crystal design. The rib width causes the broadening of the focal size in the horizontal but necessarily reduces the anticlastic bending effect that would otherwise significantly degrade diffraction resolution. The vertical profile is asymmetric and has a slow falloff at the lower side resulting from a tail on the bottom of the beam that is inherent to sagittal focusing. The FWHM of the vertical profile of the hot spot is about 170 μm, which is in very good agreement

Downloaded 19 Sep 2008 to 164.54.111.19. Redistribution subject to AIP license or copyright; see http://rsi.aip.org/rsi/copyright.jsp

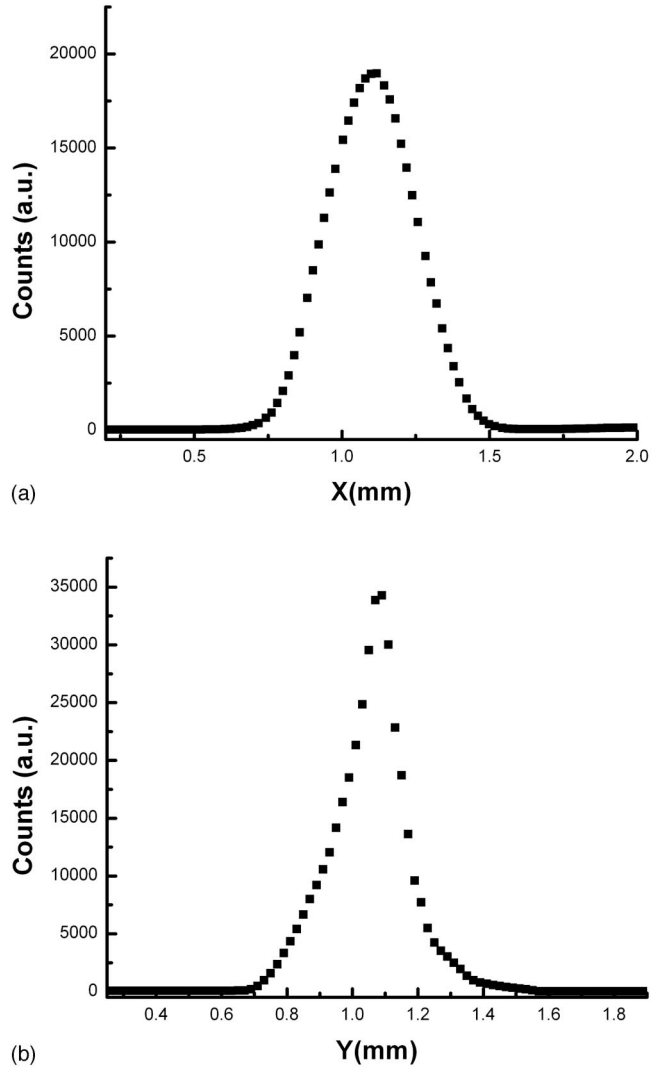

FIG. 4. Focused beam profiles at sample position in (a) horizontal and (b) vertical directions.

with its calculated value when considering the source vertical size, the mirrors' slope errors, and the focal ratio. In real sample experiments, the vertical beam focal size can be adjusted to match the sample size. The ability to focus the beam finely is very advantageous when the material being studied is available only in microgram quantities, for example, the material synthesized at high pressure.

B. Analyzer system performance

The rocking curve widths of all 12 analyzers were measured with an attenuated directed beam, as shown in Fig. 3(b). These measurements are repeated routinely to check the diffractometer performance. Initially the independent tilt adjustment was performed to optimize each analyzer, so all analyzers could have nearly identical shape and width for the rocking curve. This allows the data from all 12 detectors to be treated as equivalent, allowing the measurements to be merged and simplifying data analysis. The slight difference in reflectivity shown in Fig. 3(b) is most likely due to the different responses from the detectors and electronics. The measured rocking curve is symmetric, and the FWHM of the rocking curve is 0.005°, which is very close to the expected value.

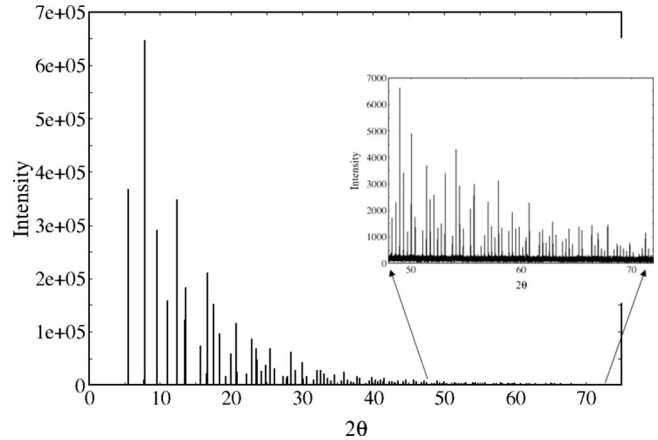

FIG. 5. High-resolution diffraction pattern from NIST standard reference material LaB_6 (660a) at 30.9 keV. The inset shows a portion of high Q data.

C. IRF

The analyzer rocking curve width could be viewed as the instrument resolution (IRF) at zero 2θ. The IRF is measured by observing diffraction peak widths as a function of 2θ. An understanding IRF allows the evaluation of the overall performance of the powder diffraction system. The IRF is also needed for microstructure studies, as it allows separation of sample-dependent diffraction profile effects from those of the instrument. An analytical expression for IRF was determined by Sabin in 1987 for multicrystal spectrometers and parallel beam optics and assuming Gaussian peak line shape.[12] Extending Sabin's work, Gozzo *et al.* developed a more general equation, which is applicable to an optical system with collimating and vertical focusing mirrors.[13] For the optical arrangements implemented in 11BM, as shown in Fig. 1, this IRF has the following form:

$$\mathrm{FWHM}(2\theta)^2 = (\Delta\tau_p^{\,2} + \Delta_m^{\,2}/2)(\tan\theta_a/\tan\theta_m - 2\tan\theta/\tan\theta_m)^2 + \Delta_a^{\,2} + \Delta_f^{\,2},$$

where $\Delta\tau_p$ is the residual source divergence after the first collimating mirror including the mirror slope error effect, Δ_f is the beam divergence after the second vertical focusing mirror including the effect from the sagittal focusing, Δ_m is the Darwin width of the monochromator crystal, and Δ_a is the Darwin width of the analyzer crystal.

Based on the equation given above, the first term has dispersive dependence as a function of 2θ, but the other two terms are constant. Therefore the shape of the IRF curve is dominated by the first term. This expression provides a guide to optimize the optics, especially the two mirrors' curvatures in order to properly collimate the beam and optimize vertical focus.

We measured instrumental profiles convoluted with those of a well-characterized sample at the 11BM instrument from diffraction pattern of the NIST LaB_6 (SRM 660a) powder. The data shown in Fig. 5 were collected at 30.9 keV with a 0.0005° 2θ step size. The intensity scale in this figure

Downloaded 19 Sep 2008 to 164.54.111.19. Redistribution subject to AIP license or copyright; see http://rsi.aip.org/rsi/copyright.jsp

is counts per second per 100 mA of ring current. A number of strong diffraction peaks over a wide 2θ range were selected and fitted individually by the CMPR program[14] where a pseudo-Voigt function was employed to describe the peak profile. The Finger–Cox–Jephcoat asymmetric function[15] did not produce significant improvement in the quality of the fits, indicating that the horizontal focusing has rendered axial divergence negligible. In order to avoid possible introduction of broadening caused by merging the 12 diffraction patterns from the multidetector system, data from a single detector were used. The FWHM of each diffraction peak, accounting for both Gaussian and Lorentzian broadening, are plotted as a function of 2θ in Fig. 6(a). These FWHMs include the sample particle size effect.

To estimate the broadening contribution due to finite crystallite size, the Lorentzian components to the psudo-Voigt FWHM were analyzed using a Williamson–Hall plot, as shown in Fig. 6(b). From this we estimate a crystallite size effect of about 0.7 μm, where d^* is as $2\sin(\theta)/\lambda$, and β^* is $\beta\cos(\theta)/\lambda$, where β is the width of the Lorentizian component of each peak.

By fitting the measured FWHMs in Fig. 6(a) using the formula given above plus the particle size effect added in quadrature, we obtained the focusing beam divergence Δ_f as 89 μrad and the residual source divergence $\Delta\tau_p$ as 7 μrad. Considering that the analyzer rocking curve width is 0.005° (87 μrad), the source vertical size σ_y is 35 μm, and the mirror slope error is 0.5 arc sec, these two fitted parameters are in good agreement with the expected values. The crystallite size parameter of 0.8 μm fitted by the Scherrer formula[16] is completely consistent with the result of the Williamson–Hall plot. In Fig. 6(c), we convert the angular units of Fig. 6(a) into reciprocal space units. At high Q values, the instrument resolution drops below the design specification of 2×10^{-4} $(\Delta Q/Q)$ to 1.7×10^{-4} without correction for the 0.8 μm crystallite size effect.

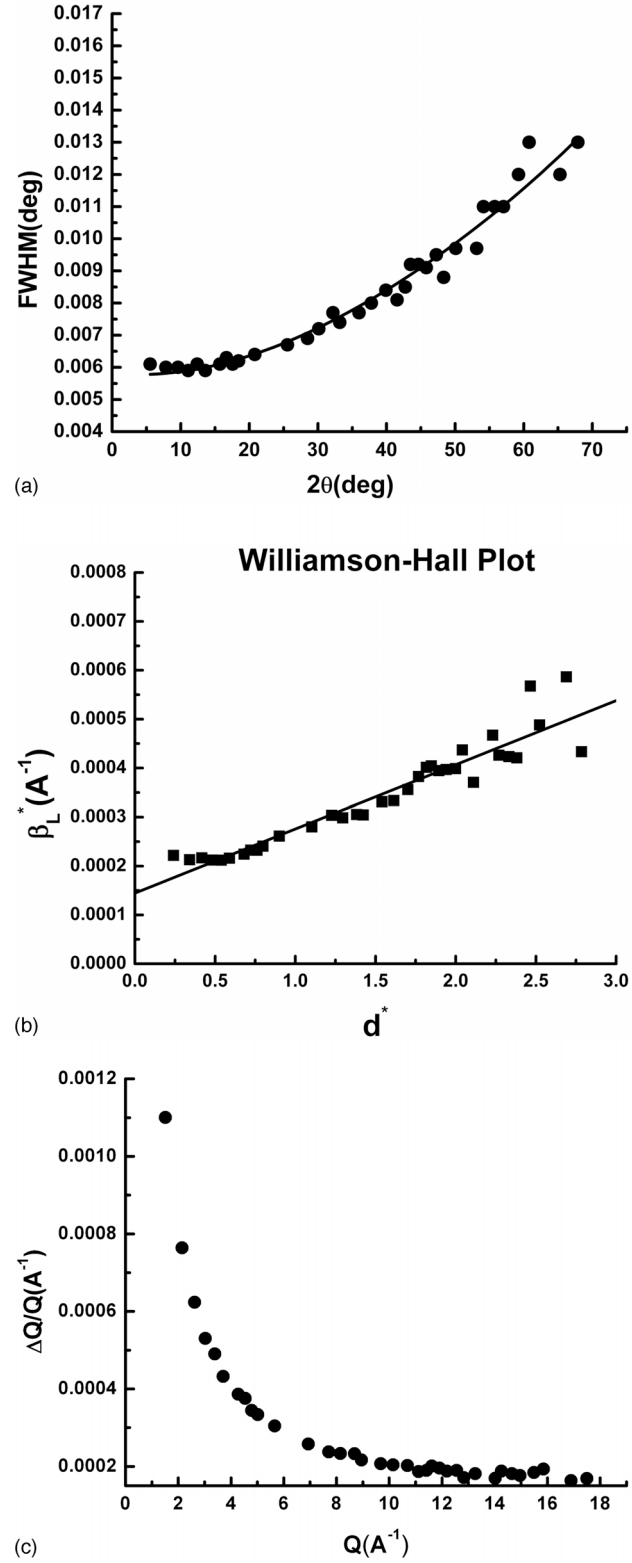

FIG. 6. (Color online) Measured FWHM of selected peaks from the 30.9 keV diffraction data shown in Fig. 5: (a) as measured (symbol) and fit (line) to the IRF, as discussed in section IVc; (b) as a Williamson–Hall plot; (c) expressed in wavelength-independent units as $\Delta Q/Q$.

D. Instrumental calibration

A mixture of NIST SRMs, $\frac{1}{3}$ Si (640c) and $\frac{2}{3}$ Al_2O_3 (676), was measured at 30.9 keV with 0.0005° step size and 30 ms counting time at each point over a range of ~60°. Its powder diffraction profile is shown as cross symbols in Fig. 7. A Rietveld[17] refinement was performed using the program GSAS[18]through EXPGUI,[19] fitting each of the 12 detectors individually. During this refinement, the only fixed parameters were the unit cell and position of Si and the polarization of the incident beam. Applying corrections for the zero offsets, scale factors, and minor differences in wavelength for each detector, it became possible to overlay and average the 12 detectors together. Even though the wavelength differences were very small (~1 eV in 30.9 keV), these corrections were absolutely necessary to avoid discrepancies in peak positions during averaging. In Fig. 7, the summed observed diffraction pattern is shown as cross symbols and is overlaid by a calculated diffraction pattern (solid line); the difference profile is shown at the bottom. The refinement statistics are $\chi^2=1.5$, $R_{wp}=6.7\%$, and $R_p=5.4\%$.

Diffraction measurements with this standard mixture can be made in half an hour or less, and the calibration refinement has been automated. The calibration parameters are recorded in a calibration data file that is then used for user data reduction.

Downloaded 19 Sep 2008 to 164.54.111.19. Redistribution subject to AIP license or copyright; see http://rsi.aip.org/rsi/copyright.jsp

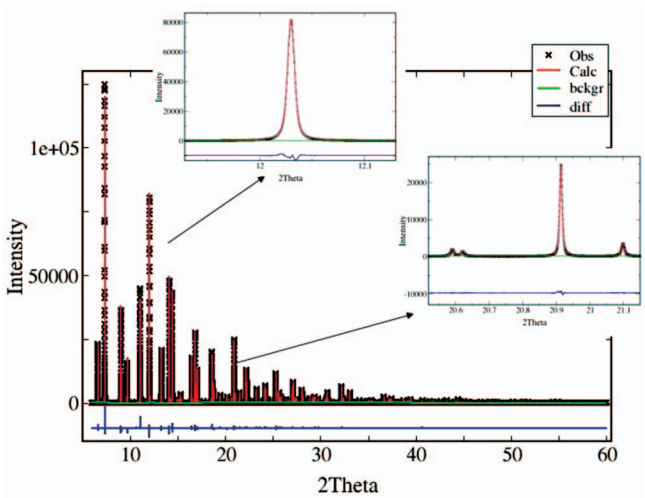

FIG. 7. (Color) Rietveld refinement using a 30.9 keV high-resolution diffraction pattern from a mixture of two NIST SRM materials [$\frac{1}{3}$ Si (640c) and $\frac{2}{3}$ Al_2O_3 (676)]. Crosses indicate averaged data from the combination of the 12 detectors, the red solid line shows the computed results, while the green line shows the fitted background. The blue line at the bottom shows the difference between the observed and computed results.

E. Instrument stability

We did a beam stability study during APS non-top-up operation mode, which refills electrons twice a day in the morning and evening. The current gradually decays from 100 to 85 mA; therefore, the worst situation will be if something was not stable due to heat load. Figure 8(a) shows a selected diffraction peak at high 2θ angle from the LaB_6 collected over the course of several hours. No position shifts were observed. However, over the course of a day and a half, minor peak position shifts were seen at high angles from the SRM mixture as shown in Fig. 8(b) while the low-angle peaks were stable [Fig. 8(c)]. The shift at a high angle of 32.115° is about 0.003°, which could be caused by a wavelength drift on the order of 1.6×10^{-5} A likely due to a beam angle drift of 2.5 μrad on the monochromator. According to our test, the drift depends primarily on the accumulated beam-on time and very little on the beam current. We think that one of the possible reasons could be the thermal expansion on the mechanical support system of the collimating mirror due to secondary scattering-induced heating.

For most of the planned experimental work, with measurements made on a time scale of hours, there would be no effect from these drifts. Measurements that seek to observe 10^{-4} level differences in lattice parameters over the course of a day or longer will need to incorporate an internal standard or make more frequent calibrations.

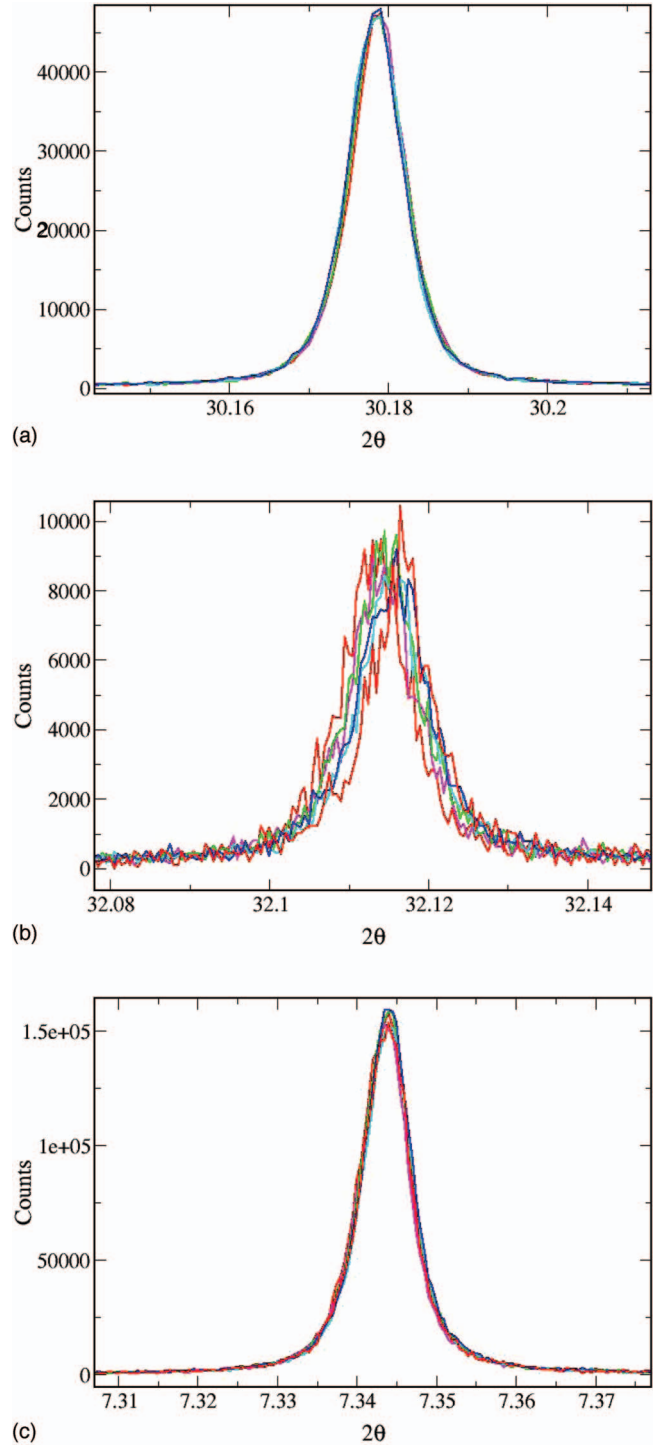

FIG. 8. (Color) Selected diffraction peaks repeatedly measured at 30.9 keV over the course of time (a) for a representative high-angle peak during a few-hours scan (LaB_6); (b) and (c) representative peaks at high angle and low angle, respectively, for 1.5 days (Si and Al_2O_3 mixture).

V. SUMMARY

The new APS 11BM beamline is dedicated to high-resolution, high-throughput powder diffraction. It has been fully commissioned and optimized. Mail-in operation within the APS general user program started in October 2007. The robotic sample changer has being running with high reliability. In order to efficiently run a high-throughput operation, we have developed and implemented web-based user interface to supply sample information that is interfaced to the instrument automation. A wide range of scientific research has been conducted at 11BM including condensed matter physics, chemistry, materials science, mineralogy, and biological and pharmaceutical sciences. Recent scientific research results are already being published.[20,21]

ACKNOWLEDGMENTS

The authors would like to acknowledge Dr. John F. Mitchell and the late Dr. James D. Jorgensen for cowriting

Downloaded 19 Sep 2008 to 164.54.111.19. Redistribution subject to AIP license or copyright; see http://rsi.aip.org/rsi/copyright.jsp

the 11BM project proposal with several of us. The instrument construction project was supported by U.S. Department of Energy, Office of Science, Office of Basic Energy Sciences, as part of DOE-BES LAB-03 instrument construction program. Use of Advanced Photon Source is supported by the U.S. Department of Energy, Office of Science, Office of Basic Energy Sciences, under Contract No. DE-AC02-06CH11357. The authors would like to thank Dr. Harriet Kung and Dr. Helen Kerch for the motivation provided by their interest in this project.

[1] I. Levin, T. A. Vanderah, R. Coutts, and S. M. Bell, J. Mater. Res. **17**, 1729 (2002).
[2] P. G. Radaelli, Y. Horibe, M. J. Gutmann, H. Ishibashi, C. H. Chen, R. M. Ibberson, Y. Koyama, Y. S. Hor, V. Kiryukhin, and S. W. Cheong, Nature (London) **416**, 155 (2002).
[3] T. Yildrim, O. Gülseren, J. W. Lynn, C. M. Brown, T. J. Udovic, Q. Huang, N. Rogado, K. A. Regan, M. A. Hayward, J. S. Slusky, T. He, M. K. Haas, P. Khalifah, K. Inumaru, and R. J. Cava, Phys. Rev. Lett. **87**, 037001 (2001).
[4] J. D. Jorgensen, D. G. Hinks, and S. Short, Phys. Rev. B **63**, 224522 (2001).
[5] Y. Zhang, P. L. Lee, G. S. Nolas, and A. P. Wilkinson, Appl. Phys. Lett. **80**, 2931 (2002).
[6] S. Pagola, P. W. Stephens, D. S. Bohle, A. D. Kosar, and S. K. Madsen, Nature (London) **404**, 307 (2000).
[7] C. J. Sparks, B. S. Borie, and J. B. Hastings, Nucl. Instrum. Methods **172**, 237 (1980).
[8] A. N. Fitch and A. Kvick, Mater. Sci. Forum **133-136**, 355 (1993).
[9] P. L. Lee, D. Shu, M. Ramanathan, C. Preissner, J. Wang, M. A. Beno, R. B. VonDreele, L. Ribaud, C. Kurtz, S. M. Antao, X. Jiao, and B. H. Toby, J. Synchrotron Radiat. **15**, 427 (2008).
[10] B. H. Toby, J. Wang, S. Antao, X. S. Jiao, and R. Von Dreele, invited talk at XXI Congress of the International Union of Crystallography (IUCr), Osaka, Japan, August 23–31 2008, (unpublished).
[11] M. Sanchez del Rio and R. Dejus, in Proceedings of the Eighth International Conference on Synchrotron Radiation Instrumentation, San Francisco, CA, 25–29 August 2003 (unpublished), pp. 784–787.
[12] T. M. Sabine, J. Appl. Crystallogr. **20**, 23 (1987).
[13] F. Gozzo, L. D. Caro, C. Giannini, A. Guagliardi, B. Schmitt, and A. Prodi, J. Appl. Crystallogr. **39**, 347 (2006).
[14] B. H. Toby, J. Appl. Crystallogr. **38**, 1040 (2005).
[15] L. W. Finger, D. E. Cox, and A. P. Jephcoat, J. Appl. Crystallogr. **27**, 892 (1994).
[16] P. Scherrer, Gott. Nachr. **2**, 98 (1918).
[17] H. M. Rietveld, J. Appl. Crystallogr. **2**, 65 (1969).
[18] A. C. Larson and R. B. Von Dreele, "General Structure Analysis System (GSAS)," Los Alamos National Laboratory Report No. LAUR 86-748, 2004.
[19] B. H. Toby, J. Appl. Crystallogr. **34**, 210.(2001).
[20] T. Varga, J. F. Mitchell, K. Yamaura, D. G. Mandrus, and J. Wang, American Physical Society March Meeting 2008, New Orleans, Louisiana.
[21] T. Varga, J. F. Mitchell, K. Yamaura, D. G. Mandrus, and J. Wang, Solid State Sci. (unpublished).

Downloaded 19 Sep 2008 to 164.54.111.19. Redistribution subject to AIP license or copyright; see http://rsi.aip.org/rsi/copyright.jsp